# The Virtual Power Feedback: Enhancing the Transient Stability of Virtual Synchronous Generators Under Current Limitation

IEEE Open Journal of
Industry Applications

Received 24 February 2025; revised 26 June 2025; accepted 2 July 2025. Date of publication 7 July 2025;
date of current version 18 July 2025.

*Digital Object Identifier 10.1109/OJIA.2025.3586412*

# The Virtual Power Feedback: Enhancing the Transient Stability of Virtual Synchronous Generators Under Current Limitation

**ALESSIA CAMBONI (Student Member, IEEE), VINCENZO MALLEMACI (Member, IEEE), FABIO MANDRILE (Member, IEEE), AND RADU BOJOI (Fellow, IEEE)**

Dipartimento Energia "G. Ferraris," Politecnico di Torino, 10129 Torino, Italy

CORRESPONDING AUTHOR: ALESSIA CAMBONI (e-mail: alessia.camboni@polito.it).

This work was supported by Project Reliable pOwer to Cloud multiKilowatt ElecTronics (ROCKET), funded by the Piedmont Region, in the framework Programma Pluriennale Attività Produttive 2018/2020 Misura "Contratto di Insediamento."

**ABSTRACT** The virtual synchronous generator (VSG) concept is a well-established control solution that facilitates the integration of power electronics-interfaced renewable sources into the electric grid. The VSG algorithm enables power converters to support the grid in case of voltage dips by injecting a large short-circuit current. However, a current limitation strategy must be implemented to address the hardware limitation of power converters. As demonstrated in the literature, the current constraint affects the VSG's dynamics by limiting the output power, thus causing a substantial acceleration of the virtual rotor and potentially leading to a loss of synchronism. Several available solutions utilize the measured actual active power as feedback, thereby modifying the VSG with complex control algorithms. On the other hand, this article proposes a different approach, highlighting the benefits of using the virtual power instead of the measured power feedback for the most adopted limitation strategies available in the literature. This paradigm shift leads to a significant improvement in stability without requiring fault detection capability or switching the control structure, as demonstrated both theoretically and experimentally in this article.

**INDEX TERMS** Current limitation, virtual synchronous generator (VSG), virtual feedback, transient stability.

## I. INTRODUCTION

In the last decades, modern power systems have faced a significant increase in integrating renewable energy sources (RES). However, the massive connection of RES to the electrical grid determines significant challenges to the power system's reliability (e.g., fault ride-through capability, lack of inertia [1], [2], [3], [4], and low-frequency oscillation [5], [6]). The virtual synchronous generator (VSG) concept represents a viable solution for power electronic-interfaced RES, such as photovoltaic and wind sources. The VSG control allows power electronic converters to provide ancillary services to the grid (e.g., inertial behaviors [1], [2], [7], [8], grid support during faults [9], [10]) by mimicking the synchronous generator (SG) dynamic. The VSG's mechanical emulation enables the converter to inject active power during frequency perturbations (i.e., inertial behaviors), thus reducing the rate of change of frequency [1], [2], [3], [4], [7], [8], [9], [10]. Furthermore, the excitation control emulation reacts to voltage variation, sustaining the grid with reactive power [9], [10]. When a voltage dip occurs, the SG emulation supports the grid by injecting a large short-circuit current several times higher than the nominal one.

However, power converters face limited current capability compared to SGs. Consequently, the power converter must be protected at the hardware level by employing current limitation techniques. Different limitation strategies are available in the literature [11], prioritizing active or reactive power injection [12], [13], [14], [15], [16], depending on the application purpose. Independently on the strategy, the VSG control faces critical stability issues during the current saturation [13], [15], [16], particularly under large voltage dips.

For this purpose, the impact of the current limitation on VSGs' transient stability has been widely studied in the technical literature, and different papers analyze the power-angle curve under current limitation conditions [13], [15], [16]. The authors in [15] and [16] have demonstrated how some current limitation strategies modify the output power-angle curve, leading to unstable operating conditions [17]. Moreover, the current limitation results in output power limitation, thus causing virtual rotor acceleration due to the difference between reference and transmissible power. This significant virtual rotor acceleration can potentially lead to the VSG's loss of synchronism.

Therefore, the literature provides numerous control solutions to avoid the VSG instability under current limitation conditions [12], [14], [18], [19], [20], [21], [22], [23], [24]. Nevertheless, most proposed solutions add complexity to the control, inserting dedicated control blocks or requiring fault detection capability [12], [21], [22], [23]. For instance, Ge et al. [21] proposed voltage and power reference variations but utilizes complex formulations that require knowledge of the grid impedance. Moreover, Ma et al. [22] modified the power feedback in the mechanical emulation according to proportional coefficients. In [23], the rotor angle or speed is saturated during a fault, impacting the quality of the ancillary services provided by the VSG concept. In addition, some of the proposed approaches consider adaptable control parameters, such as virtual inertia [18], [19], impedance [14], [20], or damping [12].

Nevertheless, the available studies only consider the transient response of VSGs using the measured active power as feedback, even though it may lead to unstable operating conditions. Indeed, the measured active power is saturated under current limitation conditions, and it features a cosine power angle curve depending on the applied limitation technique [15], [16]. Therefore, this article proposes the virtual power feedback to improve the transient stability of the VSG control. The virtual power is calculated in the control algorithm using the nonsaturated virtual current, thereby avoiding the saturation and unstable operating conditions caused by the limitation strategy.

The main contribution of this article is to demonstrate, theoretically and experimentally, the transient stability enhancement achieved thanks to the virtual power feedback. The second contribution is the calculation of the virtual power angle curves, analytically derived under different current limitation strategies. Moreover, a qualitative analysis of the virtual power angle curves is presented to evaluate the impact of the current saturation on the control's transient stability.

Notably, the VSG approach with virtual power feedback leads to the following benefits.

1) Transient stability improvement independent of the adopted current limitation strategy.
2) The same control scheme is utilized for normal and abnormal operating conditions.
3) No control parameter variation or tuning is required.
4) No fault detection algorithm is needed.

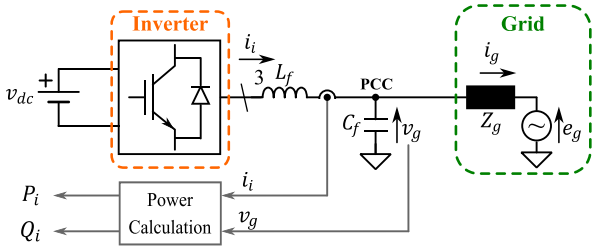


**FIGURE 1.** Schematic overview of a grid-tied inverter.

This article is an extended version of [25], in which the benefits of the virtual power feedback are theoretically and experimentally validated considering the limitation with reactive power priority. The conference paper has been modified by including the most adopted limitation strategies (i.e., limitation strategies with active power injection priority and angle priority). For each additional strategy, the following studies are presented.

1) Analytical derivation of the virtual power angle curve under current limitation conditions.
2) Qualitative transient stability analysis.
3) Experimental validation, underlining the differences in the control transient response depending on the limitation technique.

The rest of this article is organized as follows. Section II recalls the VSG model, while Section III derives the power-angle curves for the virtual active power feedback with different current saturation strategies. Section IV provides a qualitative transient stability analysis, comparing measured and virtual power feedback implementation. Then, Section V experimentally validates the improvement in transient stability with virtual power feedback. Finally, Section VI concludes this article.

## II. VSG MODEL

The system under study, schematically represented in Fig. 1, consists of a three-phase inverter connected to the grid through an $LC$ filter. The voltage at the point of common coupling (PCC) is indicated as $v_g$, whereas the grid is represented as a voltage source $e_g$ in series with its impedance $\bar{Z}_g = R_g + jX_g$. Moreover, Fig. 1 highlights the measured output powers corresponding to the powers at the inverter output.

Fig. 2 provides an overview of the VSG control scheme, which consists of three main blocks: the mechanical emulation, the excitation control, and the electrical equations. Moreover, each control block is represented in detail in Fig. 3. The control input variables are the active $P_v^*$ and reactive $Q_v^*$ power references, defined by a higher control level (i.e., droop control, maximum power point tracking). The virtual current $i_v$ is used as inverter reference current $i_i^*$. However, $i_v$ can exceed the inverter current limit $I_{\max}$ in case, for instance, of grid faults. In such a scenario, the reference current is limited to the maximum value $I_{\max}$ allowed by the inverter according to the saturation block in Fig. 2. The reference current $i_i^*$ is sent to a

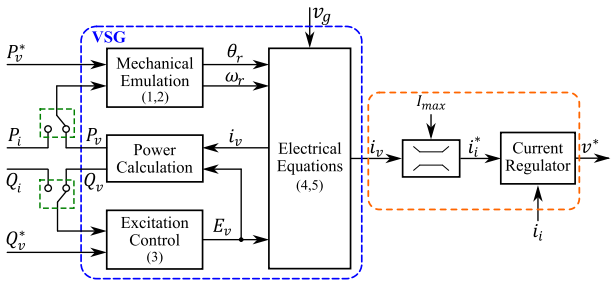


**FIGURE 2.** Overall VSG control scheme.

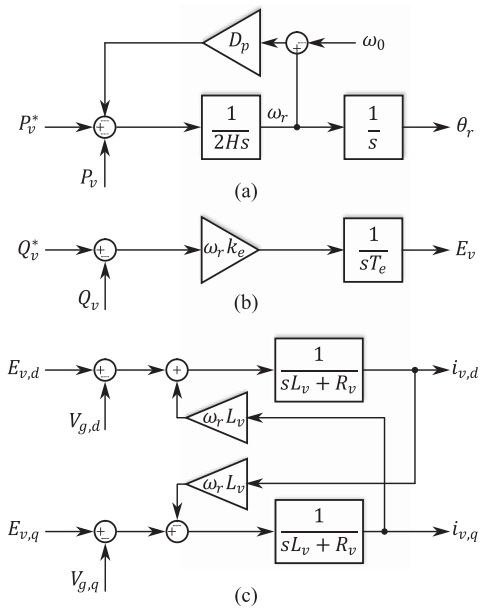


**FIGURE 3.** VSG control blocks in the continuous frequency domain. From top to bottom: (a) mechanical emulation, (b) excitation control, and (c) electrical equations.

current regulator, which controls the inverter output current $i_i$ through the voltage reference $v^*$. Note that the output current $i_i$ is limited by saturating the reference current $i_i^*$ [13], [15], [16]. Moreover, the voltage reference $v^*$ is limited to $\frac{V_{dc}}{\sqrt{3}}$, while the current regulator is equipped with an antiwindup to avoid error accumulation on the integral part [26], [27].

Starting from the mechanical emulation in Fig. 3(a), the swing equation (1) mimics the mechanical behavior according to the inertia constant $H$. Furthermore, the damping strategy is droop-based and implemented through the factor $D_p$, tuned based on [28]. The mechanical emulation sets the virtual angular speed $\omega_r$ considering the variation from the nominal grid angular speed $\omega_0$ (i.e., $\omega_r = \Delta\omega_r + \omega_0$). Moreover, the virtual angle $\theta_r$ is calculated from the angular speed $\omega_r$ as in (2). The excitation control (3) in Fig. 3(b) defines the electromotive force amplitude $E_v = \Delta E_v + E_{v0}$ depending on the time constant $T_e$ and gain $k_e$, set according to [29]

$$P_v^* - P_v = 2H\frac{d\Delta\omega_r}{dt} + D_p\Delta\omega_r \tag{1}$$

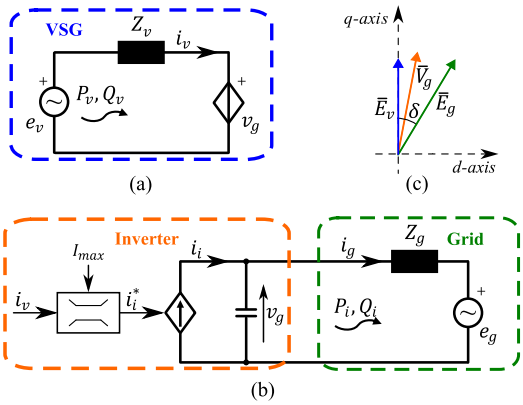


**FIGURE 4.** (a) VSG equivalent circuit with virtual power feedback $\mathbf{P_v}$ and $\mathbf{Q_v}$. (b) Inverter-grid side equivalent circuit. (c) Vectorial representation of the virtual voltage $\bar{\mathbf{E}}_\mathbf{v}$, PCC voltage $\bar{\mathbf{V}}_\mathbf{g}$, and grid voltage $\bar{\mathbf{E}}_\mathbf{g}$.

$$\frac{d\theta_r}{dt} = \Delta\omega_r + \omega_0 \tag{2}$$

$$Q_v^* - Q_v = \frac{T_e}{\omega_r k_e}\frac{d\Delta E_v}{dt}. \tag{3}$$

The VSG control acts as a voltage source in series with its virtual impedance $\bar{Z}_v = R_v + jX_v$, tuned according to [30], [31]. Indeed, the electrical equations in the synchronous reference frame are (4) and (5). Moreover, the reference currents $i_{v,d}$ and $i_{v,q}$ are obtained from (4) and (5), as shown in Fig. 3(c)

$$e_{v,d} - v_{g,d} = R_v i_{v,d} - \omega_r L_v i_{v,q} + L_v\frac{di_{v,d}}{dt} \tag{4}$$

$$e_{v,q} - v_{g,q} = R_v i_{v,q} + \omega_r L_v i_{v,d} + L_v\frac{di_{v,q}}{dt}. \tag{5}$$

As shown in Fig. 2, the swing equation (1) and the excitation control (3) utilize the virtual power $P_v$ and $Q_v$ as feedback, calculated inside the VSG control through the terms $e_v$ and $i_v$ according to [10]. Moreover, a selector allows changing the power feedback in (1) and (3) with the measured powers $P_i$ and $Q_i$, respectively. Note that the selector will be employed to experimentally test the transient response of the VSG when using either the virtual feedback or the measured one.

The equivalent circuit in Fig. 4 represents a grid-tied inverter with the VSG control, described by two equivalent circuits coupled via the PCC voltage $v_g$.

1) As illustrated in Fig. 4(a), the VSG control can be represented as a voltage source $e_v$ connected to the PCC, with voltage $v_g$, through its virtual impedance $Z_v$, as widely demonstrated in the literature [7], [8], [10], [12], [15], [16], [22], [28], [29]. Indeed, the virtual current $i_v$ is obtained from the electrical equations (4) and (5), as shown in Fig. 3(c).
2) The output circuit, in Fig. 4(b), represents the connection between the inverter and the grid. The inverter operates as a controlled current source. Indeed, the controlled variable is the inverter current $i_i$, as depicted in

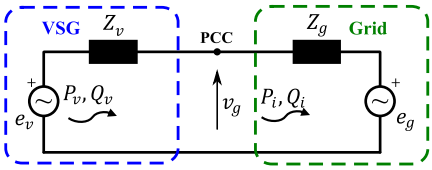


**FIGURE 5.** Equivalent circuit of a grid-tied inverter with VSG control in normal operating conditions.

Fig. 2 [10], [15], [16], [20], [28], [29]. The voltage $v_g$ depends on the output current $i_i$ and the grid voltage $e_g$.

Note that the adopted output circuit representation allows for direct analysis of both the normal and current limitation conditions [15], [16]. As shown in Fig. 4(c), the virtual voltage $\bar{E}_v$ is considered aligned with the $q$-axis, while $\delta$ is the phase shift between $\bar{E}_v$ and the grid voltage $\bar{E}_g$. Moreover, the virtual power $P_v$ is the power at the virtual voltage source $e_v$, whereas the output one $P_i$ is the power at the inverter output, as underlined in Fig. 4.

As it can be noted in Fig. 4(b), the reference current $i_i^*$ and the virtual one $i_v$ are equal if $|i_v| \leq I_{\max}$, i.e., normal operating condition. Otherwise, the virtual current $i_v$ still flows in the virtual circuit with no limitation, whereas the inverter injects the limited inverter current $|i_i^*| = I_{\max}$.

Note that the $LC$ filter dynamic is neglected to study the transient response of the VSG control due to the different time scales (i.e., $i_i \approx i_g$). Moreover, the current regulator is assumed to accurately track the reference current (i.e., $i_i \approx i_i^*$) [13], [15], [16].

In normal operating conditions, the overall equivalent circuit in Fig. 4 evolves into the circuit in Fig. 5. According to the circuit in Fig. 5, the virtual power can be calculated as in (6) [32], where $\bar{Z}_t = R_t + jX_t = (R_v + R_g) + j(X_v + X_g)$

$$P_v = \frac{R_t}{Z_t^2}E_v^2 - \frac{R_t}{Z_t^2}E_vE_g\cos(\delta) + \frac{X_t}{Z_t^2}E_vE_g\sin(\delta). \quad (6)$$

Considering $R_t \ll X_t$ (i.e., medium or high voltage connection), the expression in (6) can be approximated as follows:

$$P_v \approx \frac{1}{X_t}E_vE_g\sin(\delta) = \frac{1}{X_v + X_g}E_vE_g\sin(\delta). \quad (7)$$

In normal operating conditions, utilizing the virtual power rather than the measured power feedback does not affect the VSG control, being $P_v$ and $P_i$ equivalent except for the voltage drop on $\bar{Z}_v$. Note that the active power reference $P^*$ can be modified by adding the term $R_v i_i^2$ to compensate for the virtual losses, thus obtaining equal virtual $P_v$ and actual powers $P_i$ in normal operating conditions.

## III. CURRENT LIMITATION TECHNIQUES

This section analyzes the system behavior when the VSG control operates in current limitation conditions, considering three different limitation techniques available in the literature [12], [13], [14], [15], [16]. The virtual power-angle curves are derived for each saturation strategy to evaluate the VSG transient stability with virtual power feedback.

Let us consider a scenario where a large symmetrical voltage sag occurs. The VSG algorithm reacts with a virtual current $i_v$ that exceeds the maximum allowed value. Consequently, the control enters the saturation condition, limiting the output current (i.e., $i_v \neq i_i^* = i_i$). Indeed, virtual $P_v$ and output $P_i$ powers differ under current limitation conditions.

1) The output power $P_i$ is limited as it depends on the saturated output current $i_i$.
2) The virtual power $P_v$ at the virtual voltage source is not limited, as it depends on the nonsaturated virtual current $i_v$.

Since the swing equation (1) utilizes the virtual feedback, the virtual angle response depends on the $P_v$ characteristic [33]. Therefore, the equivalent circuits in Fig. 4 must be solved when $i_v \neq i_i$ to analyze the VSG transient stability.

On the inverter-grid side circuit, the saturated output current is generally indicated as $i_i$ for the different limitation techniques. The PCC voltage $v_g$ can be expressed in the $(d, q)$ frame, rotating at $\omega_r$, as a function of the inverter current $i_i$ and the grid voltage $e_g$. Note that $\omega_r$ is approximated as equal to one in (8) and (9) [16]. Moreover, the $dq$-components of the grid voltage can be expressed in terms of the rotor angle $\delta$ by following the vectorial representation in Fig. 4(c) (i.e., $e_{g,d} = E_g\sin(\delta)$, and $e_{g,q} = E_g\cos(\delta)$)

$$v_{g,d} = -X_g i_{i,q} + R_g i_{i,d} + e_{g,d} \quad (8)$$

$$v_{g,q} = X_g i_{i,d} + R_g i_{i,q} + e_{g,q}. \quad (9)$$

According to the VSG equivalent circuit in Fig. 4(a), the virtual current $i_v$ can be expressed in terms of $e_v$ and $v_g$ as follows. For the detailed calculation, refer to the Appendix

$$i_{v,d} = \frac{R_v}{Z_v^2}e_{v,d} + \frac{X_v}{Z_v^2}e_{v,q} - \frac{R_v}{Z_v^2}v_{g,d} - \frac{X_v}{Z_v^2}v_{g,q} \quad (10)$$

$$i_{v,q} = \frac{R_v}{Z_v^2}e_{v,q} - \frac{X_v}{Z_v^2}e_{v,d} - \frac{R_v}{Z_v^2}v_{g,q} + \frac{X_v}{Z_v^2}v_{g,d}. \quad (11)$$

Therefore, the virtual active power $P_v$ is calculated according to (12), where the electromotive force vector is aligned with the $q$-axis (i.e., $e_{v,q} = E_v$ and $e_{v,d} = 0$), as underlined in Fig. 4(c)

$$P_v = e_{v,q}i_{v,q} = \frac{R_v}{Z_v^2}E_v^2 - \frac{R_v}{Z_v^2}E_v v_{g,q} + \frac{X_v}{Z_v^2}E_v v_{g,d}. \quad (12)$$

Next, the virtual active power can be expressed as in (13) by replacing (8) and (9) into (12), where the terms $P_{\text{sat}}$ and $P_\delta$ are as in (14) and (15), respectively

$$P_v = P_{\text{sat}} + P_\delta \quad (13)$$

$$P_{\text{sat}} = \frac{R_v}{Z_v^2}E_v\left(-X_g i_{i,d} - R_g i_{i,q}\right) + \frac{X_v}{Z_v^2}E_v\left(-X_g i_{i,q} + R_g i_{i,d}\right) \quad (14)$$

$$P_\delta = \frac{R_v}{Z_v^2}E_v^2 - \frac{R_v}{Z_v^2}E_vE_g\cos(\delta) + \frac{X_v}{Z_v^2}E_vE_g\sin(\delta). \quad (15)$$

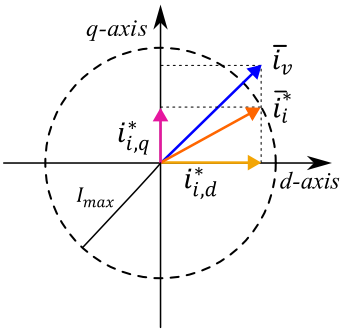


**FIGURE 6.** Vectorial representation of the current references with *d*-axis priority technique (i.e., reactive power priority).

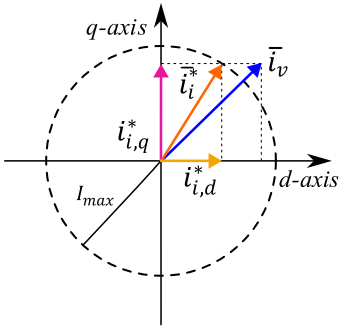


**FIGURE 7.** Vectorial representation of the current references with *q*-axis priority technique (i.e., active power priority).

Conceptually, the virtual power $P_v$ can indeed be divided into two contributions, $P_{\text{sat}}$ and $P_\delta$.

1) The component $P_{\text{sat}}$ represents the current limitation effect and depends on the applied limitation technique.
2) The term $P_\delta$ coincides with the active power exchange between the virtual generator $e_v$ and the grid $e_g$ through the virtual impedance $Z_v$ as if no current limitation is applied.

Therefore, the saturation condition generates an additional power component $P_{\text{sat}}$, varying the term $P_\delta$. The effect of $P_{\text{sat}}$ is analyzed in the following sections, considering the different limitation techniques available in the literature [12], [13], [14], [15], [16] that are described in the following sections.

### A. D-AXIS PRIORITY

This limitation strategy saturates the reference current module $|i_i^*|$ to $I_{\max}$, prioritizing its reactive component, as shown in (16). The resulting current vector $\bar{i}_i^*$ is schematically represented in Fig. 6

$$\begin{cases} |i_{i,d}^*| &= \min\left(|i_{v,d}|, I_{\max}\right) \\ |i_{i,q}^*| &= \min\left(|i_{v,q}|, \sqrt{I_{\max}^2 - i_{i,d}^{*2}}\right). \end{cases} \tag{16}$$

When the current module reaches the maximum allowed value $I_{\max}$, the saturated components become as follows:

$$|i_{i,d}^*| = I_{\max}, \quad |i_{i,q}^*| = 0. \tag{17}$$

By replacing (17) in (14), the virtual power component $P_{\text{sat}}^d$ results, as shown in the following equation:

$$P_{\text{sat}}^d = -\frac{R_v}{Z_v^2} E_v \left(X_g I_{\max}\right) + \frac{X_v}{Z_v^2} E_v \left(R_g I_{\max}\right). \tag{18}$$

Assuming $R_v + R_g \ll X_v + X_g$, the effect of the saturation condition can be neglected, thus determining a virtual active power $P_v^d$ as in the following equation:

$$P_v^d \approx P_\delta = \frac{1}{X_v} E_v E_g \sin(\delta). \tag{19}$$

Assuming the condition in (17), the expression in (20) compares the virtual power $P_v^d$ and the measured one $P_i^d$. As pointed out in [15] and [16], the output power $P_i^d$ faces a significant limitation in the maximum transmissible power as it depends on the saturated output current

$$\begin{cases} P_v^d &= \frac{1}{X_v} E_v E_g \sin(\delta) \\ P_i^d &= I_{\max} E_g \sin(\delta). \end{cases} \tag{20}$$

### B. Q-AXIS PRIORITY

Complementary to the previous one, this strategy limits the *q*-component of the reference current to the maximum allowed value $I_{\max}$, prioritizing the active power injection, as shown in (21). Fig. 7 illustrates the current reference $\bar{i}_i^*$ when applying the *q*-axis priority technique

$$\begin{cases} |i_{i,d}^*| &= \min\left(|i_{v,d}|, \sqrt{I_{\max}^2 - i_{i,q}^{*2}}\right) \\ |i_{i,q}^*| &= \min\left(|i_{v,q}|, I_{\max}\right). \end{cases} \tag{21}$$

When $|i_{v,q}| \geq I_{\max}$, the reference current components are set as in (22). Therefore, the virtual power component $P_{\text{sat}}^q$ can be expressed as in (23) by combining (22) and (14)

$$|i_{i,d}^*| = 0, \quad |i_{i,q}^*| = I_{\max} \tag{22}$$

$$P_{\text{sat}}^q = -\frac{R_v}{Z_v^2} E_v \left(R_g I_{\max}\right) - \frac{X_v}{Z_v^2} E_v \left(X_g I_{\max}\right). \tag{23}$$

Differently from the previous case, $P_{\text{sat}}^q$ still plays a role in the virtual power flow when neglecting the resistive part. Notably, the current saturation affects the virtual power exchange between $e_v$ and $e_g$ by reducing it through the term $P_{\text{sat}}^q$, as expressed in the following equation:

$$P_v^q = P_{\text{sat}}^q + P_\delta = -\frac{X_g}{X_v} E_v I_{\max} + \frac{1}{X_v} E_v E_g \sin(\delta). \tag{24}$$

Nevertheless, the obtained virtual power shows a sinusoidal characteristic, whereas the output power $P_i^q$ has a cosine behavior [15], [16], as expressed in the following equation:

$$\begin{cases} P_v^q &= -\frac{X_g}{X_v} E_v I_{\max} + \frac{1}{X_v} E_v E_g \sin(\delta) \\ P_i^q &= I_{\max} E_g \cos(\delta). \end{cases} \tag{25}$$

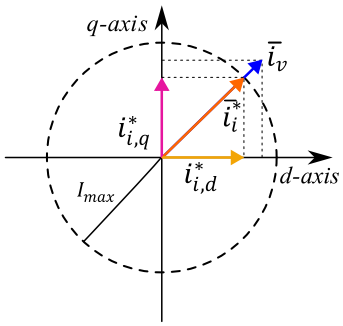


**FIGURE 8.** Vectorial representation of the current references with angle priority technique.

### C. ANGLE PRIORITY

Contrary to the previous ones, this limitation technique prioritizes the angle of the reference current vector [15], [16] (i.e., the magnitude is limited while preserving the angle of the reference current vector), as schematically represented in Fig. 8. Therefore, the magnitude of the reference current vector is limited to $I_{\max}$ rather than individually prioritizing the $dq$-components, as expressed in the following equation:

$$\begin{cases} |i^*_{i,d}| &= \min\left(|i_{v,d}|, |i_{v,d}|\dfrac{I_{\max}}{\sqrt{i^2_{v,d}+i^2_{v,q}}}\right) \\ |i^*_{i,q}| &= \min\left(|i_{v,q}|, |i_{v,q}|\dfrac{I_{\max}}{\sqrt{i^2_{v,d}+i^2_{v,q}}}\right) \end{cases}. \tag{26}$$

In this case, the saturated output current $i_i$ is not independent of the virtual one $i_v$. Therefore, the application of (14) is not straightforward.

Let us simplify the virtual power calculation by introducing the term $\zeta_{\text{sat}}$, expressed in the following equation:

$$\zeta_{\text{sat}} = \frac{\sqrt{i^2_{v,d}+i^2_{v,q}}}{I_{\max}}. \tag{27}$$

Next, the PCC voltage in the $(d, q)$ frame can be written as in (28) and (29)

$$v_{g,d} = -\frac{X_g}{\zeta_{\text{sat}}} i_{v,q} + \frac{R_g}{\zeta_{\text{sat}}} i_{v,d} + e_{g,d} \tag{28}$$

$$v_{g,q} = \frac{X_g}{\zeta_{\text{sat}}} i_{v,d} + \frac{R_g}{\zeta_{\text{sat}}} i_{v,q} + e_{g,q}. \tag{29}$$

The VSG equivalent circuit in Fig. 4(a) can be solved, thus obtaining the virtual current $i_v$ as follows:

$$i_{v,d} = \frac{R_{\text{sat}}}{Z^2_{\text{sat}}} e_{v,d} + \frac{X_{\text{sat}}}{Z^2_{\text{sat}}} e_{v,q} - \frac{R_{\text{sat}}}{Z^2_{\text{sat}}} v_{g,d} - \frac{X_{\text{sat}}}{Z^2_{\text{sat}}} v_{g,q} \tag{30}$$

$$i_{v,q} = \frac{R_{\text{sat}}}{Z^2_{\text{sat}}} e_{v,q} - \frac{X_{\text{sat}}}{Z^2_{v}} e_{v,d} - \frac{R_{\text{sat}}}{Z^2_{\text{sat}}} v_{g,q} + \frac{X_{\text{sat}}}{Z^2_{\text{sat}}} v_{g,d} \tag{31}$$

where $Z_{\text{sat}}$ is defined as in (32)

$$\bar{Z}_{\text{sat}} = R_{\text{sat}} + jX_{\text{sat}} = \left(R_v + \frac{R_g}{\zeta_{\text{sat}}}\right) + j\left(X_v + \frac{X_g}{\zeta_{\text{sat}}}\right). \tag{32}$$

Therefore, the virtual active power $P^a_v$ results, as shown in the following equation:

$$P^a_v = \frac{R_{\text{sat}}}{Z^2_{\text{sat}}} E^2_v - \frac{R_{\text{sat}}}{Z^2_{\text{sat}}} E_v E_g \cos(\delta) + \frac{X_{\text{sat}}}{Z^2_{\text{sat}}} E_v E_g \sin(\delta). \tag{33}$$

The obtained expression shows that the angle priority technique acts as an impedance variation on the virtual power flow $P^a_v$. Notably, the equivalent impedance $Z_{\text{sat}}$ features the following aspects:

1) varies with $\zeta_{\text{sat}}$ (i.e., depends on the operating condition);
2) the coefficient $\zeta_{\text{sat}}$ is always higher or equal than 1 (i.e., $|i_i| \leq |i_v|$), meaning that $X_v < X_{\text{sat}} \leq (X_v + X_g)$.

Furthermore, the virtual active power can be approximated as (34) by assuming negligible resistance

$$P^a_v = \frac{1}{X_{\text{sat}}} E_v E_g \sin(\delta). \tag{34}$$

Indeed, the virtual active power $P^a_v$ is still characterized by a sinusoidal trend. On the contrary, the angle priority results in a cosinusoidal output power exchange $P^a_i$ [15], [16], as expressed in the following equation:

$$\begin{cases} P^a_v &= \dfrac{1}{X_{\text{sat}}} E_v E_g \sin(\delta) \\ P^a_i &= I_{\max} E_g \cos\left(\dfrac{\delta}{2}\right). \end{cases} \tag{35}$$

## IV. CURRENT LIMITATION EFFECT ON TRANSIENT STABILITY

This section qualitatively analyzes the transient stability of the VSG control under current limitation conditions through power-angle curve considerations. The different limitation strategies are presented separately for the same fault condition, comparing the actual and virtual power characteristics. Moreover, the nonlimited power-angle curve is considered for the qualitative analyzes to highlight the impact of the current saturation.

### A. D-AXIS PRIORITY

Assuming the saturation condition in (17), the $P^d_v$ characteristic corresponds to the active power exchange between the virtual generator $e_v$ and the grid $e_g$ through the only virtual impedance $Z_v$. Therefore, the virtual active power does not depend on the grid impedance $Z_g$. When $|i_{i,d}| = I_{\max}$ and $|i_{i,q}| = 0$, the resulting power-angle curve differs from the ones available in the literature (e.g., [13], [15], [16], [21]) in the following two main aspects.

1) The reactance involved in the power transmission is only the virtual one $X_v$, thus determining a higher maximum transmissible power in current saturation

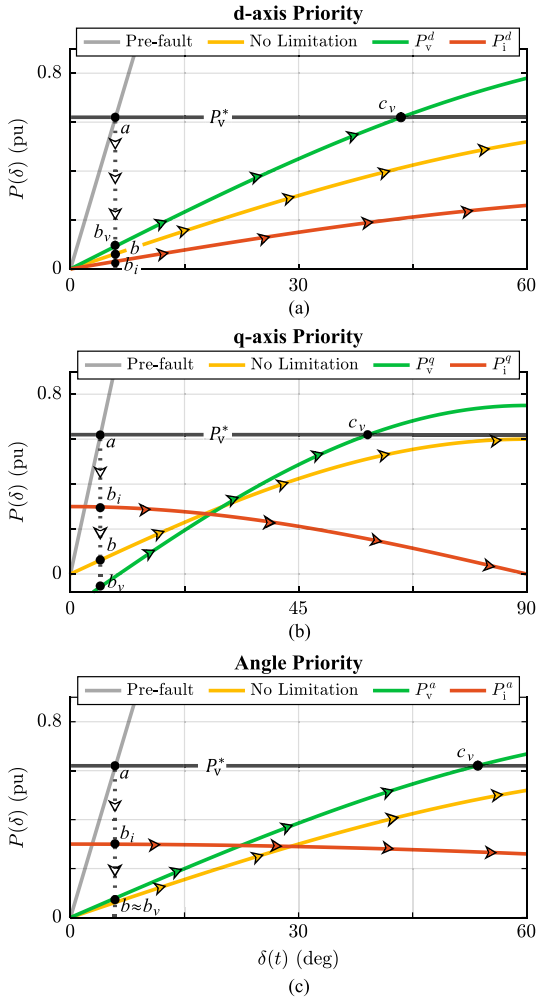


**FIGURE 9.** Examples of system trajectory in fault condition during a large voltage sag for (a) *d*-axis, (b) *q*-axis, and (c) angle priority techniques. The power-angle curves are: prefault curve in grey, no current limitation in yellow, current limitation with virtual feedback $\mathbf{P_v}$ in green, and current limitation with measured feedback $\mathbf{P_i}$ in red.

than in no limitation conditions (i.e., $\frac{1}{X_v}E_vE_g\sin(\delta) > \frac{1}{X_v+X_g}E_vE_g\sin(\delta)$).

2) When using the actual measured power $P_i^d$ as feedback and under current saturation conditions, the maximum transmissible power is limited to $I_{\max}E_g$ [15], [16].

Fig. 9(a) shows an example of power-angle curves for a symmetrical voltage sag considering the saturation condition in (17). During the prefault condition, the control operates at point $a$. Then, the system follows the power-angle characteristic in the fault condition. The system trajectory differs for the following three power-angle curves in Fig. 9(a) as follows.

1) The virtual rotor continues accelerating when utilizing the saturated actual power feedback $P_i^d$ (red curve), and in the no-limitation case (yellow curve), due to the impossibility of reaching the power reference;
2) When utilizing the virtual feedback $P_v^d$ (green curve), the control can virtually inject the required power (i.e., an intersection exists between $P_v^d$ and $P_v^*$) thanks to the higher power-angle curve. Therefore, the system settles on the stable equilibrium point $c_v$.

When considering a higher reference $P_v^*$, the VSG with virtual feedback cannot inject the required power, and the rotor accelerates during the fault. Nevertheless, the saturated virtual power $P_v^d$ (green curve) achieves the highest transmissible power, determining the lowest rotor angle acceleration, i.e., transient stability improvement.

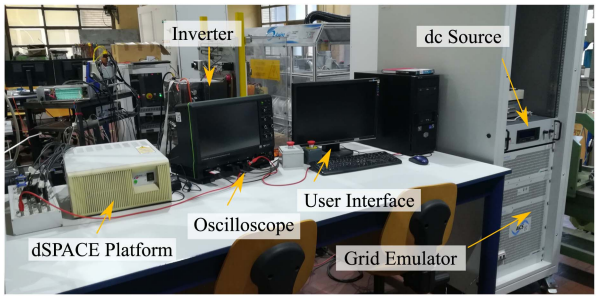


**FIGURE 10.** Experimental setup.

### B. Q-AXIS PRIORITY

As derived in Section III-B, the $q$-axis priority reduces the virtual power exchange through the term $P^q_{\text{sat}}$ if $|i_{v,q}| \geq I_{\max}$. Nevertheless, the total virtual power $P_v^q$ characteristic features the following aspects.

1) When using the virtual power feedback $P_v^q$, the $q$-axis technique results in a sinusoidal virtual power-angle curve. On the contrary, the actual output power $P_i^q$ follows a cosine waveform, as derived in [15] and [16].
2) The maximum transmissible power $\max(P_v^q)$ can be higher than in nonsaturation conditions, depending on the fault scenario and system parameters.

By imposing (36), the condition for a higher maximum transmissible power can be retrieved as follows:

$$\begin{aligned} &\max\left(P_v^q\right) > \max\left(P_v\right) \Rightarrow \\ &-\frac{X_g}{X_v}E_vI_{\max} + \frac{1}{X_v}E_vE_g > \frac{1}{X_v+X_g}E_vE_g. \end{aligned} \tag{36}$$

From (36), the relation (37) is derived. More in detail, the condition in (37) shows that the $q$-axis saturation condition determines a lower or higher virtual power depending on the grid reactance (i.e., lower with a weak grid and higher with a strong grid)

$$X_v < \frac{E_g}{I_{\max}} - X_g. \tag{37}$$

Fig. 9(b) indeed shows an example where the system virtually injects a higher maximum power $\max(P_v^q)$ in saturation (green curve) than in a nonsaturation condition $\max(P_v)$ (yellow curve). As shown in Fig. 9(b), the negative term's impact is higher for small-angle operations (i.e., $P_v^q(\delta) < 0$ if $\delta \approx 0$). Depending on the angle operating conditions, the virtual power can be lower or higher than in the case without

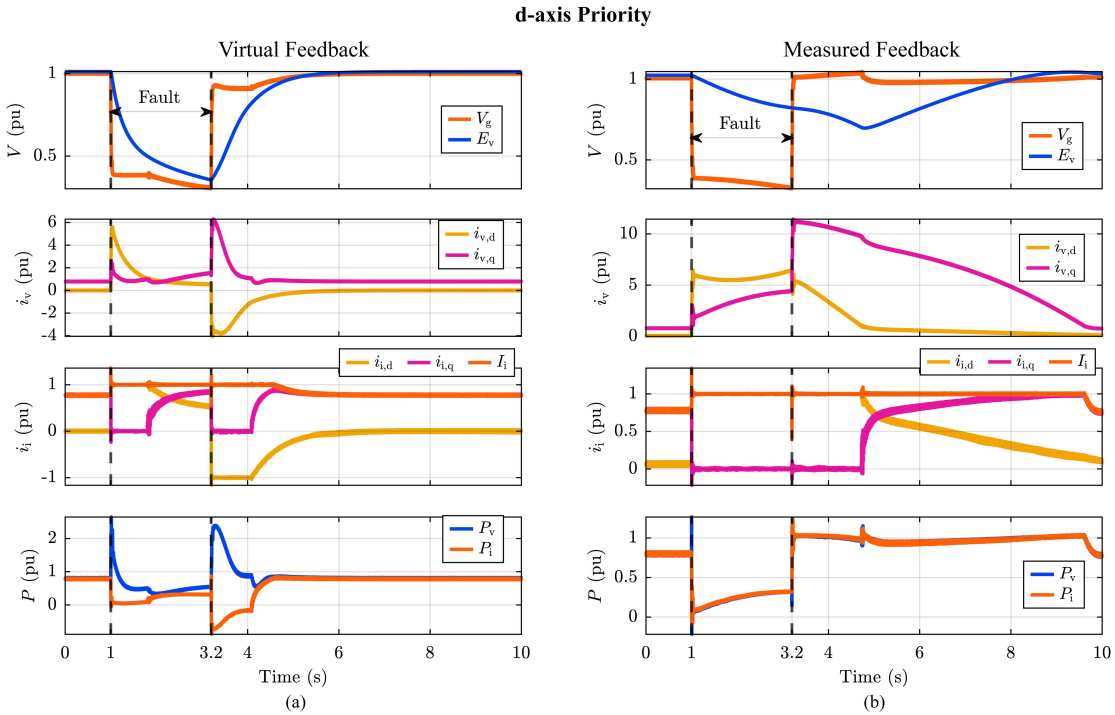


**FIGURE 11.** *d*-axis priority. Experimental results for a symmetrical voltage sag of −0.7 p.u. and 2.2 s with (a) virtual feedback and (b) measured feedback. From top to bottom: voltage amplitude at PCC $V_g$ and virtual electromotive force amplitude $E_v$, nonsaturated reference currents $i_v$ in $(d, q)$ frame, $dq$ output current $i_{i,dq}$ and output current amplitude $I_i$, virtual power $P_v$, and measured power $P_i$.

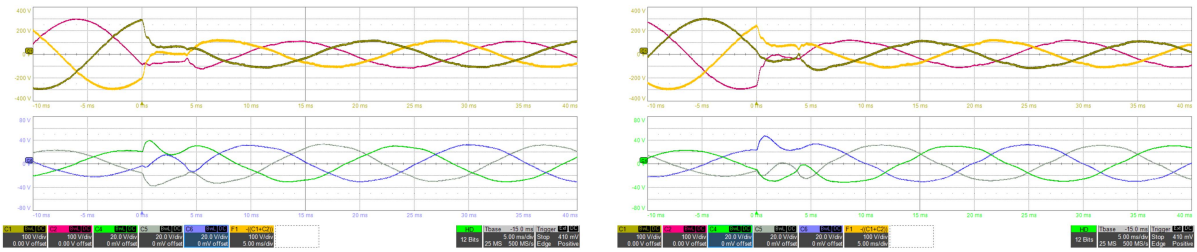


**FIGURE 12.** *d*-axis priority. Experimental results for a symmetrical voltage sag of −0.7 p.u. and 2.2 s with (a) virtual feedback, and (b) measured feedback. From top to bottom: line to line three-phase PCC voltage (C1, C2, F1) and three-phase grid current $i_g$ (C4, C5, C6).

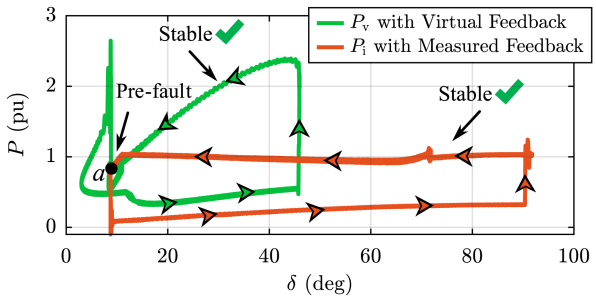


**FIGURE 13.** *d*-axis priority. Virtual power $P_v$ and measured power $P_i$ to the variation of the rotor angle $\delta$ for a symmetrical voltage sag of −0.7 p.u. and 2.2 s.

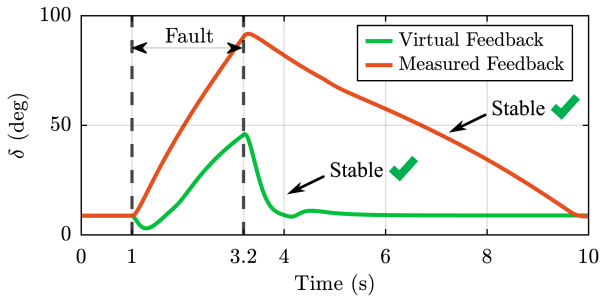


**FIGURE 14.** *d*-axis priority. Rotor angle $\delta$ dynamic with measured and virtual power feedback for a symmetrical voltage sag of −0.7 p.u. and 2.2 s.

limitation. Therefore, a lower rotor angle acceleration is not guaranteed for the $q$-axis priority technique.

For the scenario in Fig. 9(b), an intersection exists between the power reference and the virtual power angle curve (green curve). Therefore, the virtual rotor accelerates and settles in

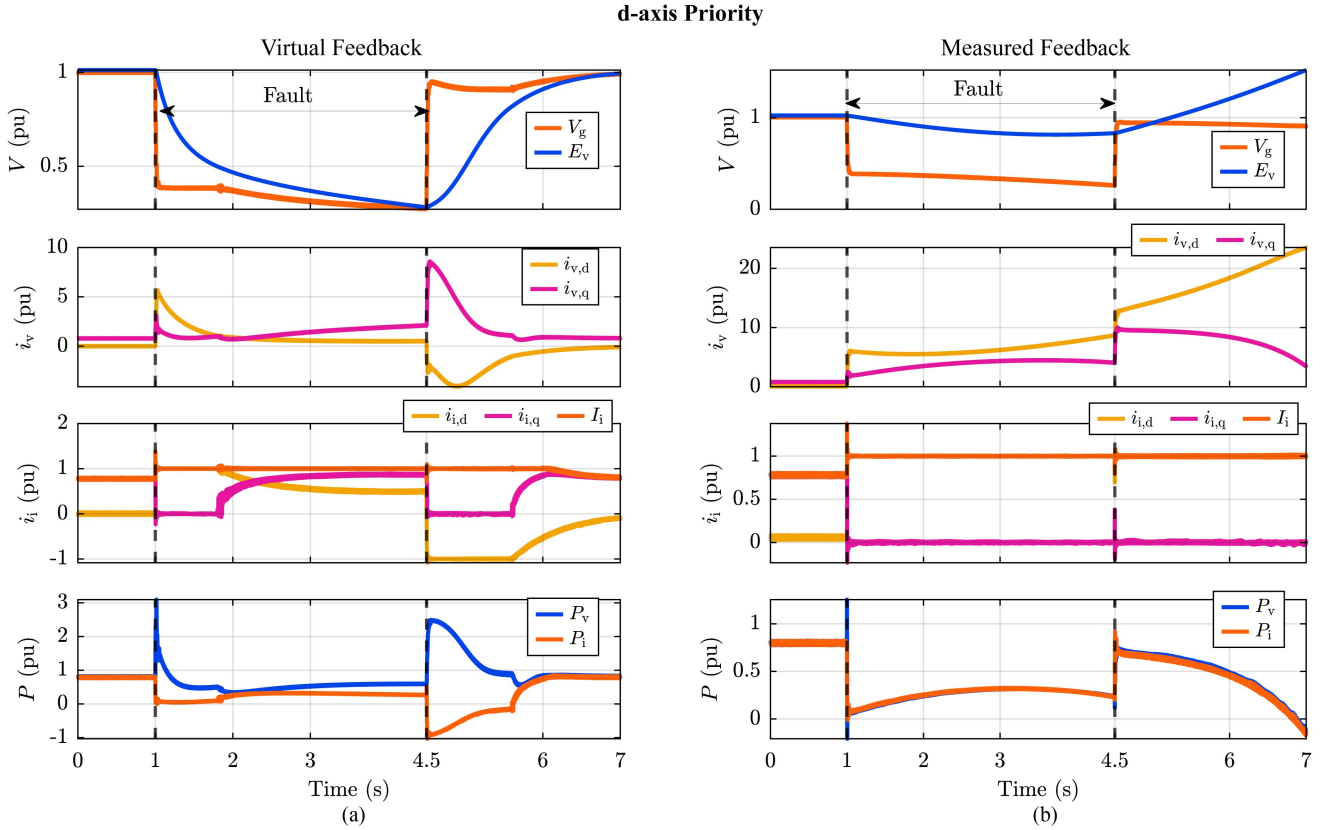


**FIGURE 15.** *d*-axis priority. Experimental results for a symmetrical voltage sag of −0.7 p.u. and 3.5 s with virtual (a) feedback and (b) measured feedback. From top to bottom: voltage amplitude at PCC $V_g$ and virtual electromotive force amplitude $E_v$, nonsaturated reference currents $i_v$ in ($d$, $q$) frame, $dq$ output current $i_{i,dq}$ and output current amplitude $I_i$, virtual power $P_v$, and measured power $P_i$.

the stable equilibrium point $c_v$ when utilizing the virtual feedback. Note that the rotor accelerates during the fault if a higher power reference is set, both in nonlimited conditions (yellow curve) and with virtual feedback (green curve).

When considering the measured feedback, the $q$-axis priority leads to a cosinusoidal output power $P_i^q$ (red curve) if $|i_{i,q}| = I_{\max}$, as represented in Fig. 9(b). When the fault occurs, the system moves to the point $b_i$. Then, the rotor angle increases while the transmissible power decreases (i.e., positive feedback in the control [34]). The saturation condition with the feedback $P_i^q$ indeed determines the control operation in the unstable power-angle area. Consequently, the VSG control with the $P_i^q$ feedback must be modified to avoid the loss of synchronism [18], [19], [20], [21], [22], [23].

Therefore, the virtual power feedback improves the VSG's transient stability also when applying the $q$-axis limitation technique.

### C. ANGLE PRIORITY

As discussed in Section III-C, the angle priority technique affects the equivalent impedance between the virtual voltage generator $e_v$ and the grid $e_g$. Moreover, the saturated impedance $Z_{\text{sat}}$ is not constant but depends on $\zeta_{\text{sat}}$, whose lowest value is 1 (i.e., $|i_i| = |i_v| = I_{\max} \Rightarrow X_{\text{sat}} = X_v + X_g$).

Therefore, the resulting virtual power $P_v^a$ during the angle priority limitation is characterized by the following aspects.

1) The equivalent reactance in the virtual power transmission is $X_{\text{sat}} \leq X_v + X_g$. Therefore, the virtual power during the saturation condition is higher or equal than without saturation;
2) The virtual power $P_v^a$ still features a sinusoidal behavior, while the actual output power $P_i^a$ a cosinusoidal one [15], [16].

Fig. 9(c) provides an example where $\zeta_{\text{sat}}$ is equal to 3. With the virtual feedback and angle priority (green curve), the control can inject the required active power during the fault. Note that the stable equilibrium point existence is not guaranteed but depends on the parameter $\zeta_{\text{sat}}$. For $\zeta_{\text{sat}} = 1$, $P_v^a$ indeed coincides with the power-angle curve without limitation (yellow curve); hence, the system cannot reach a stable point. Therefore, the rotor angle accelerates during the fault both for limitation with virtual feedback and without limitation. Nonetheless, the limitation condition with the $P_v^a$ feedback (green curve) allows lower or equal rotor angle acceleration thanks to the higher transmissible power.

The same considerations for the output power with $q$-axis limitation are valid for the angle priority strategy. With the measured power feedback $P_i^a$ (red curve), the control indeed operates in the unstable area independently

of the power reference value. Therefore, the VSG algorithm must be modified with additional blocks to avoid unstable operating conditions [18], [19], [20], [21], [22], [23].

Once again, the virtual power feedback improves the control transient response with the angle priority technique.

### D. CONCLUSIVE REMARKS

As stated in Section II, the virtual power $P_v$ represents the power at the virtual voltage generator $e_v$. Therefore, the virtual feedback is not saturated even under current limitation conditions, thus enhancing the transient response under a fault. Moreover, the virtual power $P_v$ features a sinusoidal power angle curve for the three limitation strategies, thereby avoiding unstable operating conditions for low values of the rotor angle (i.e., $\delta < \frac{\pi}{2}$).

In contrast with the measured power, the virtual power $P_v$ depends on the virtual reactance $X_v$ (i.e., $\omega_v L_v$), although the output current is saturated, as derived in Section III. Even though a lower $X_v$ value increases the virtual power, a variation of $L_v$ can cause synchronization issues when the fault is cleared. Therefore, the virtual inductance $L_v$ is not modified during the fault.

Note that the virtual and output power are zero if a short-circuit occurs at the PCC. Therefore, utilizing virtual or measured feedback does not affect the system's response during the fault, as both powers are equal to zero. Nevertheless, the virtual power feedback is also beneficial in a short-circuit scenario. Indeed, the overall transient response depends both on the fault and postfault power-angle curve [35]: the higher the power, the larger the potential energy in the postfault. Therefore, the control features a larger potential energy capability to lead the system back to synchronism when utilizing the virtual power feedback rather than the measured one. The advantages of the virtual power feedback are valid for any of the three limitation strategies analyzed so far.

## V. EXPERIMENTAL VALIDATION

The VSG transient stability has been evaluated considering the system illustrated in Fig. 1. Moreover, the experimental setup is shown in Fig. 10 and consists of a 7.5 kVA, three-phase, two-level inverter connected to a grid emulator through an *LC* filter. Moreover, the output filter parameters are designed according to [27], [36]. The inverter is supplied by an ideal DC source and controlled through the dSPACE platform. The main system and control parameters are summarized in Table 1.

Based on the qualitative analyses in Section IV, the virtual power feedback is expected to improve the VSG's transient response for the three limitation techniques presented so far. Therefore, the system dynamic is evaluated for the VSG control with virtual and measured power feedback during a fault. More in detail, the test consists of applying a symmetrical voltage sag of $-0.7$ p.u. for 2.2 s while observing the VSG response with a current limitation of $I_{\max} = 1$ p.u. Before the fault occurrence, the VSG works at $P_v = 0.8$ p.u. and $Q_v = 0$ p.u. Moreover, the postfault condition coincides with the complete restoration of the grid voltage (i.e., $E_g = 1$ p.u.).

**TABLE 1. Experimental Setup Parameters**

| Inverter | | Base Values | | Grid | |
|---|---|---|---|---|---|
| $S_N$ | 7.5 kVA | $S_{base}$ | 7.5 kVA | $\widehat{V}_g$ | $120\sqrt{2}$ V |
| $I_N$ | 30 A | $V_{base}$ | $120\sqrt{2}$ V | $L_g$ | 0.0720 p.u. |
| $f_{sw}$ | 10 kHz | $\omega_{base}$ | 314 rad/s V | $R_g$ | 0.0131 p.u. |
| **VSM** | | | | ***LC* Filter** | |
| $L_v$ | 0.1 p.u. | $D_p$ | 267.6 p.u. | $L_f$ | 0.0297 p.u. |
| $R_v$ | 0.02 p.u. | $T_e$ | 0.5 s | $C_f$ | 0.0398 p.u. |
| $H$ | 10 s | $k_e$ | 0.344 p.u. | | |

### A. EXPERIMENTS FOR D-AXIS PRIORITY

Fig. 11(a) shows the overall experimental results for the VSG control with virtual power feedback and $d$-axis current limitation strategy. During the prefault operating condition, virtual and measured active powers coincide and are equal to the power reference $P_v^* = 0.8$ p.u. At the fault occurrence, the voltage amplitude at the three-phase PCC $V_g$ quickly decreases, as shown in Fig. 11(a). Moreover, the excitation control emulation reduces the voltage amplitude at the virtual generator $E_v$ according to the time constant $T_e$ of the excitation control. In more detail, Fig. 12(a) provides the PCC line-to-line voltage and grid current $i_g$ within 40 ms from the fault occurrence.

When the fault occurs, the VSG reacts to the voltage variation by generating reactive reference current $i_{v,d}$ to support the grid. Due to the fault's occurrence, the control enters the limitation condition, saturating $i_{i,d}$ to $I_{\max}$, as shown in Fig. 11(a). Consequently, the virtual active power $P_v$ differs from the output one $P_i$, as the system behaves according to the equivalent circuit discussed in Section II. When $i_{i,d} = I_{\max}$ and $i_{i,q} = 0$, the virtual power indeed follows the curve expressed in (19), resulting in a higher transmissible power, as shown in Fig. 11(a).

In the postfault condition, the excitation control still tries to inject a high reactive current component because of the voltage difference between the virtual generator $E_v$ and the grid $E_g$, thus determining the VSG's operation in the current limitation condition. After the fault, the control returns to the prefault state within 1.8 s (i.e., $P_v = P_i = 0.8$ p.u).

On the other hand, the VSG can operate using the measured output powers $P_i$ and $Q_i$ as feedback in (1) and (3), respectively. Fig. 11(b) depicts the system response for the same fault condition as before. The control with measured feedback reacts as with virtual feedback when observing the first instants after the fault occurrence. As shown in Fig. 12(b), the PCC voltage quickly reduces, determining the reactive current injection and the control operation under the saturation condition $i_{i,d} = I_{\max}$ and $i_{i,q} = 0$. Contrary to the previous

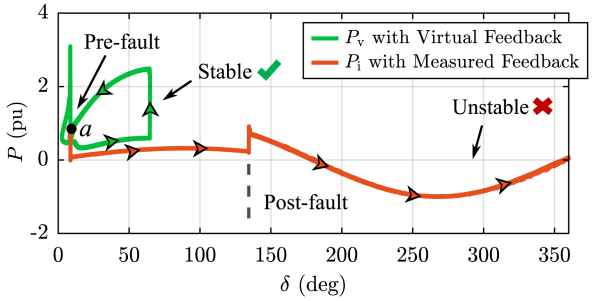


**FIGURE 16.** *d*-axis priority. Virtual power $P_v$ and measured power $P_i$ to the variation of the rotor angle $\delta$ for a symmetrical voltage sag of −0.7 p.u. and 3.5 s.

test, the virtual and output power coincide when utilizing the measured output power feedback. Furthermore, the saturation condition $i_{i,d} = I_{\max}$ and $i_{i,q} = 0$ persists throughout the fault, significantly limiting the output power. At the fault clearance, the system slowly returns to the prefault state within 6.5 s.

Fig. 13 depicts the virtual $P_v$ and measured $P_i$ power to the variation of the rotor angle, thereby comparing the different power-angle trajectories where point $a$ indicates the prefault condition. As shown in Fig. 13, the output power-angle characteristic that rules the system's dynamic is significantly limited in transmissible power when using the measured power feedback. Therefore, the difference between the reference $P_v^*$ and the transmissible power causes a high acceleration of the rotor angle, as shown in Fig. 14. Consequently, the measured power feedback determines a broader trajectory in the power-angle frame, leading to a slower recovery in the postfault. On the other hand, the virtual power feedback features a higher transmissible power during the current saturation. Therefore, the rotor angle accelerates significantly less for the same fault condition, as expected from Section IV-A.

Next, the test is repeated for a symmetrical voltage sag of −0.7 p.u. and 3.5 s. Even with a prolonged voltage sag, the VSG with virtual feedback returns to the stable condition during the postfault, as shown in Fig. 15(a). On the contrary, the limited output power leads to the loss of synchronism when applying the same type of fault to the VSG with measured power feedback, as depicted in Fig. 15(b). Consequently, the control with the output feedback slowly oscillates following the power-angle curve in Fig. 16.

Nonetheless, the VSG with virtual feedback cannot inject the required power during the fault, thus causing the rotor angle acceleration, as illustrated in Fig. 16. The fault duration is prolonged to experimentally observe how long the VSG with virtual feedback can withstand the fault, returning to the synchronism in the postfault condition. As depicted in Fig. 17, the loss of synchronism occurs after a 7 s fault. In this scenario, the rotor angle accelerates so that the control cannot maintain the synchronism in the postfault, as shown in Fig. 17. Nevertheless, this result demonstrates the remarkable improvement in transient stability achieved by implementing the virtual feedback. Notably, the high virtual power-angle curve allows the control to ride through

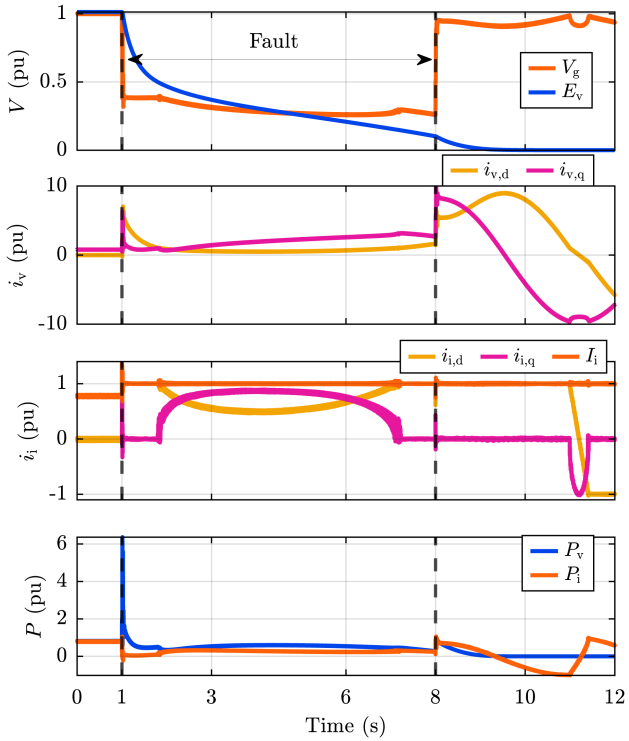


**FIGURE 17.** *d*-axis priority. Experimental results for a symmetrical voltage sag of −0.7 p.u. and 7 s with virtual feedback. From top to bottom: voltage amplitude at PCC $V_g$ and virtual electromotive force amplitude $E_v$, nonsaturated reference currents $i_i$ in $(d, q)$ frame, $dq$ output current $i_{i,dq}$ and amplitude $I_i$, virtual power $P_v$, and measured power $P_i$.

the fault for 3.5 s longer than when utilizing the measured feedback.

### B. EXPERIMENTS FOR Q-AXIS PRIORITY

The $q$-axis strategy is implemented in the VSG control with the virtual feedback, resulting in the transient response, as shown in Fig. 18(a). The system operates in the same prefault condition as before when a symmetrical voltage sag of −0.7 p.u. is applied for 2.2 s. During the first second of the fault, the VSG control has some current margin to inject reactive power through the term $i_{i,d}$. Then, the control enters the saturation condition $i_{i,q} = I_{\max}$ and $i_{i,d} = 0$, which persists until 1 s after the fault clearance. In this limitation condition, $P_v^q$ follows the characteristic derived in Section III-B, while the $P_i^q$ curve is cosinusoidal [15], [16]. When the fault is cleared, the system returns to the prefault state within 2 s, after which $P_v$ and $P_i$ are again equal.

The $q$-axis technique is then applied to the VSG control with measured power feedbacks $P_i$ and $Q_i$ to observe the control response for the same fault condition. Right after the fault occurrence, the output current is saturated to $i_{i,q} = I_{\max}$ and $i_{i,d} = 0$. As pointed out in [15] and [16], this saturation condition determines a cosinusoidal output power characteristic. The output power behavior can be better observed in Fig. 19, where the power-angle curves are displayed. The measured power indeed decreases while the rotor angle increases, thus leading to the control instability and loss of synchronism in

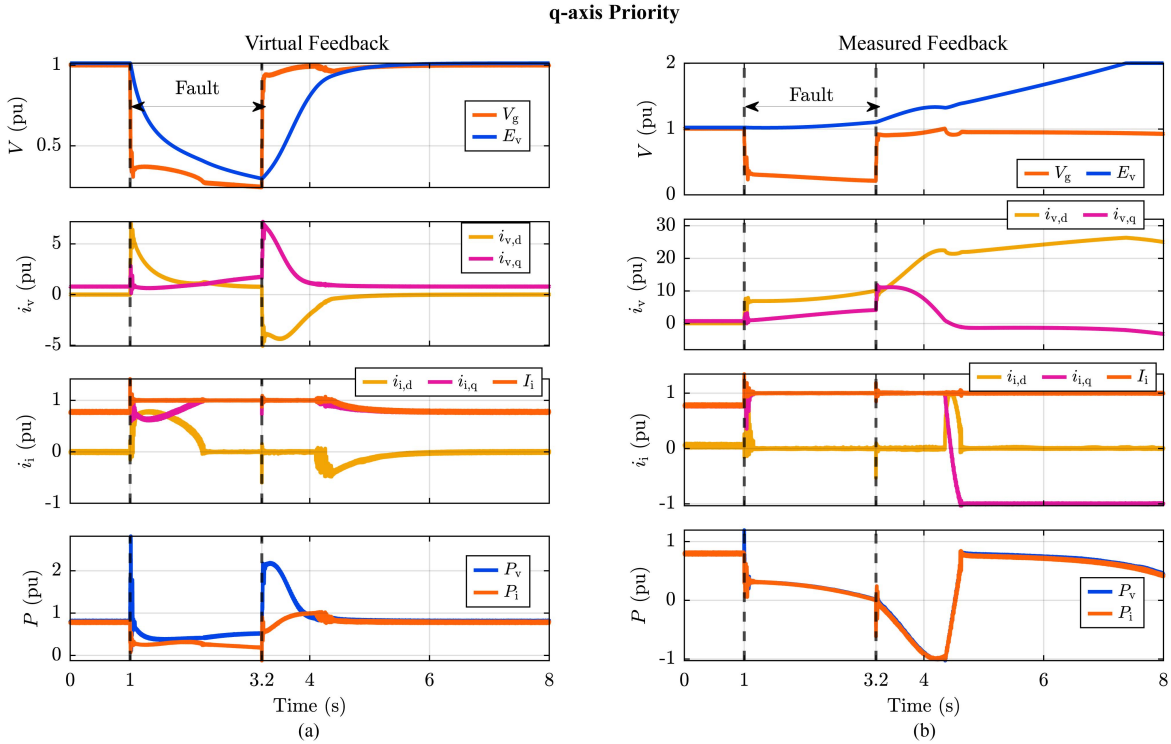


**FIGURE 18.** *q*-axis priority. Experimental results for a symmetrical voltage sag of −0.7 p.u. and 2.2 s with (a) virtual feedback and (b) measured feedback. From top to bottom: voltage amplitude at PCC $V_g$ and virtual electromotive force amplitude $E_v$, nonsaturated reference currents $i_v$ in $(d, q)$ frame, $dq$ output current $i_{i,dq}$ and output current amplitude $I_i$, virtual power $P_v$, and measured power $P_i$.

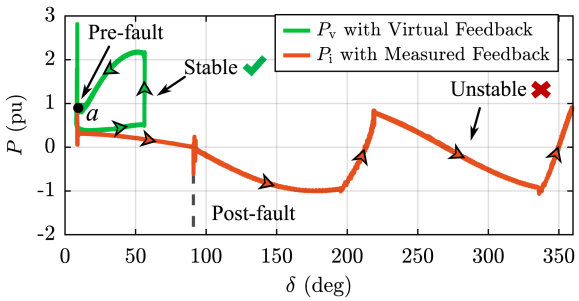


**FIGURE 19.** *q*-axis priority. Virtual power $P_v$ and measured power $P_i$ to the variation of the rotor angle $\delta$ for a symmetrical voltage sag of −0.7 p.u. and 2.2 s.

the postfault, as depicted in Fig. 18(b). Therefore, additional control strategies must be implemented to operate with the $q$-axis limitation and output power feedback $P_i$ [18], [19], [20], [21], [22], [23]. On the other hand, the VSG with virtual feedback returns to the stable equilibrium point in postfault, as shown in Fig. 19. Therefore, the virtual feedback significantly improves the VSG transient stability also when applying the $q$-axis priority strategy.

### C. EXPERIMENTS FOR ANGLE PRIORITY

The system is then tested using the angle priority strategy and virtual power feedback. Fig. 20(a) illustrates the experimental results obtained for a symmetrical voltage sag of −0.7 p.u. applied for 2.2 s. As discussed in Section III-C, this limitation strategy saturates the output current, prioritizing the angle. Therefore, the output current components $i_{i,dq}$ follow the virtual ones $i_{v,dq}$, rescaled in terms of amplitude, as shown in Fig. 20(a). Consistent with Section III, the virtual and output powers are different when the control operates in limitation conditions. Furthermore, the virtual power is higher than the measured one throughout the fault. Once the fault is cleared, the system returns to the prefault state after 1.8 s.

Next, the VSG control with the output power feedback $P_i$ is tested under angle priority limitation when applying the same fault. As depicted in Fig. 21, the VSG with measured power determines a significantly higher rotor angle acceleration, which reaches around 90° at the fault clearance. Then, the virtual rotor continues to accelerate while the output power decreases consistently with the studies in [15] and [16]. The saturated output power behavior rules the control response, leading to the loss of synchronism in the postfault condition, as illustrated in Fig. 20(b).

Conversely, the virtual power feedback allows the system to return to synchronism after the fault, as shown in Fig. 21. Hence, implementing virtual power feedback enhances the VSG's transient response also with angle priority limitation.

### D. FINAL CONSIDERATIONS

The VSG control transient dynamic varies depending on the limitation techniques due to the different virtual power angle curves derived in Section III. Therefore, Fig. 22 compares the virtual rotor angle response obtained from the experimental

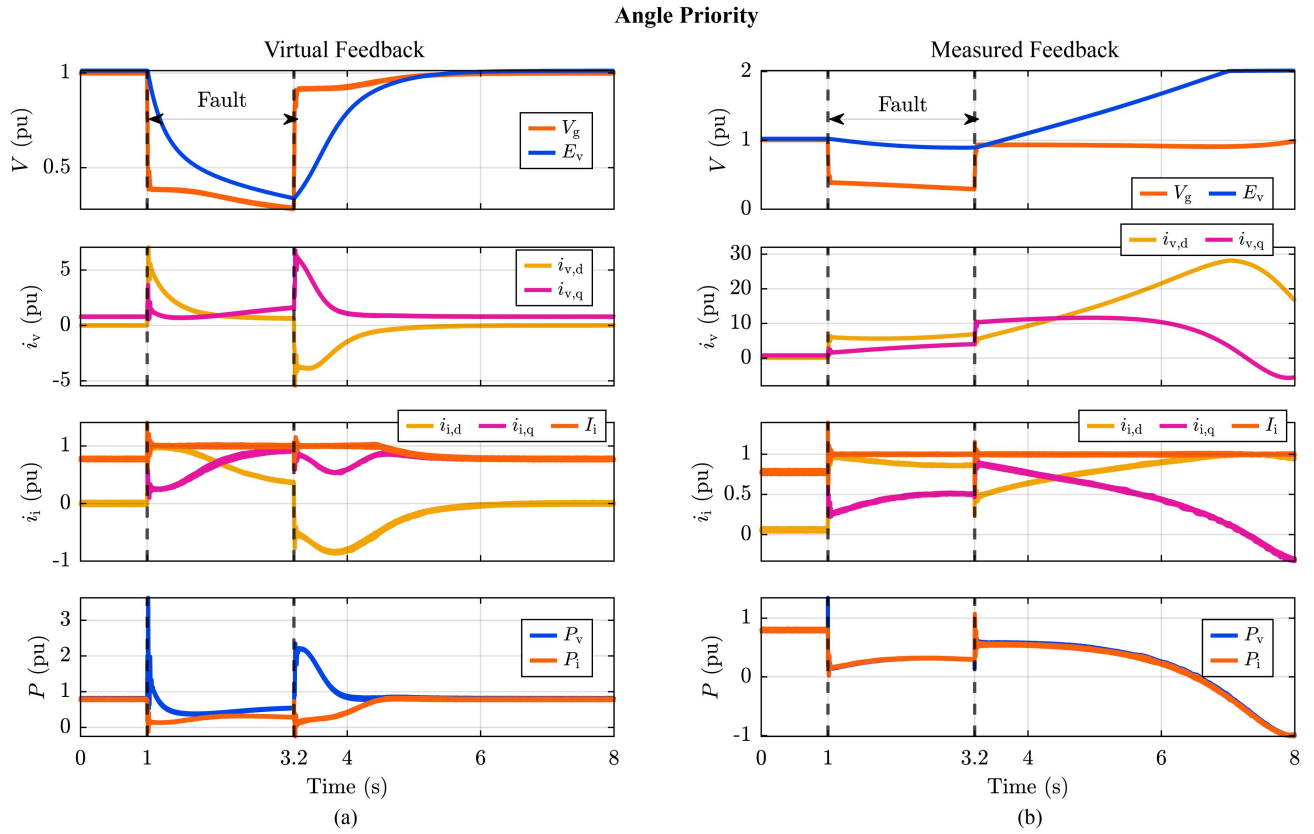


**FIGURE 20.** Angle priority. Experimental results for a symmetrical voltage sag of −0.7 p.u. and 2.2 s with (a) virtual feedback and (b) measured feedback. From top to bottom: voltage amplitude at PCC $V_g$ and virtual electromotive force amplitude $E_v$, nonsaturated reference currents $i_v$ in $(d, q)$ frame, $dq$ output current $i_{i,dq}$ and output current amplitude $I_i$, virtual power $P_v$, and measured power $P_i$.

**TABLE 2.** Comparison of the Virtual and Measured Power Feedback for the Three Limitation Strategies

| Type of limitation | *d*-axis Priority | | *q*-axis Priority | | Angle Priority | |
|---|---|---|---|---|---|---|
| Type of feedback | Proposed Virtual Feedback | Conventional Measured Feedback | Proposed Virtual Feedback | Conventional Measured Feedback | Proposed Virtual Feedback | Conventional Measured Feedback |
| 2s Voltage Dip | Stable | Stable | Stable | Unstable | Stable | Unstable |
| Sinusoidal Power-Angle Curve | ✓ | ✓ | ✓ | × | ✓ | × |
| Higher Power-Angle Curve than Ideal Scenario | ✓ | × | – | × | ✓ | × |

validation for the three limitation strategies to observe the different control responses. Furthermore, Fig. 22 considers the rotor angle dynamic without current limitation, obtained from a PLECS simulation, to comprehensively evaluate the analysis carried out in Section IV.

As expected from Section IV-A, the $d$-axis technique results in the lowest rotor angle acceleration thanks to the highest transmissible virtual power. Note that the rotor angle accelerates more if no limitation is applied. This result is consistent with Section III-A, which demonstrates that the virtual power flow with the $d$-axis limitation is only dominated by the virtual reactance $X_v$ when $|i_{i,d}| = I_{\max}$.

With the angle priority technique, the virtual power is higher or equal to the nonlimitation scenario, as demonstrated in Section III-C. Therefore, the control results in a similar rotor angle response for the cases with and without limitation. Furthermore, the virtual power flow depends on $X_{\text{sat}} > X_v$, thus leading to a lower transmissible power than the $d$-axis priority strategy (i.e., higher rotor angle acceleration).

The $q$-axis technique leads to the highest rotor angle acceleration, as illustrated in Fig. 22. This experimental result aligns with the theoretical one in Section III-B, which shows how the virtual power flow obtained with the $q$-axis is lower than that with $d$-axis saturation.

Moreover, Fig. 23 depicts the experimental virtual power $P_v$ to the variation of the rotor angle $\delta$, comparing the theoretical power-angle curves derived in Section III. For $d$-axis and $q$-axis priority strategies, the theoretical expressions are valid when $|i_{i,d}| = I_{\max}$ and $|i_{i,q}| = I_{\max}$, respectively. As can be seen from Fig. 23, the experimental results are consistent with

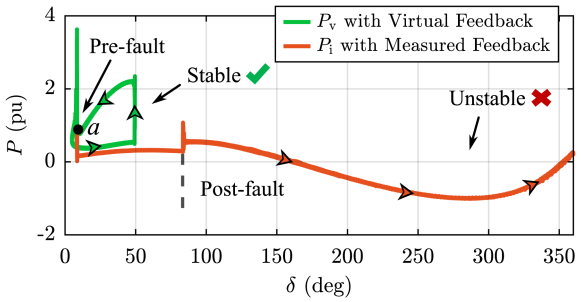


**FIGURE 21.** Angle priority. Virtual power $P_v$ and measured power $P_i$ to the variation of the rotor angle $\delta$ for a symmetrical voltage sag of $-0.7$ p.u. and 2.2 s.

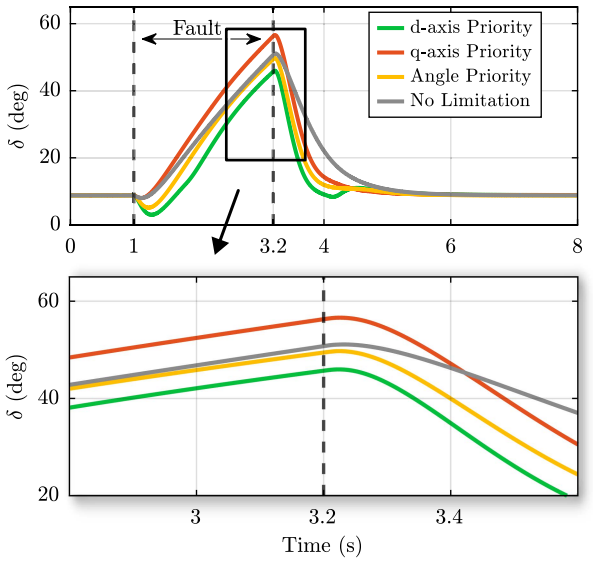


**FIGURE 22.** Comparison of the rotor angle $\delta$ dynamic for VSG with virtual feedback when applying: $d$-axis technique in green, $q$-axis technique in red, angle priority in yellow and no-limitation in grey.

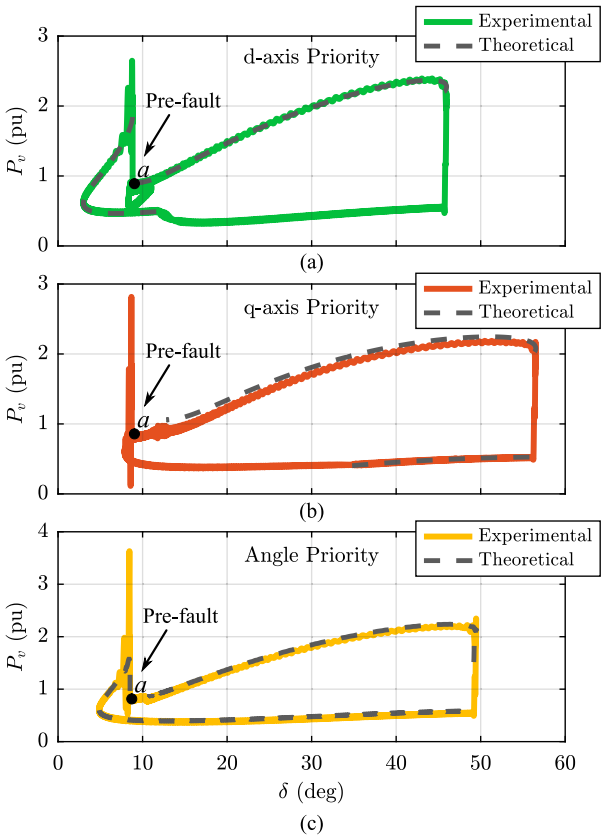


**FIGURE 23.** Virtual power $P_v$ to the variation of the rotor angle $\delta$: comparison between experimental results (solid line) and theoretical power-angle curves (dashed line). From top to bottom: (a) $d$-axis priority in green, (b) $q$-axis priority in red, and (c) angle priority in yellow.

the theoretical ones for the three limitation strategies, thus validating the analysis in Section III.

From the theoretical analysis and experimental validation, the following advantages emerge for the VSG control with virtual power feedback.

1) For the $d$-axis technique, the virtual power-angle curve is higher than the actual output power characteristic, thus achieving a remarkably lower rotor angle acceleration for the same fault condition.
2) The $d$-axis technique modifies the equivalent reactance that rules the virtual power flow in the saturation condition $i_{i,d} = I_{\max}$. The power exchange indeed only depends on the virtual reactance, hence, independent of the grid reactance.
3) The virtual power under the $q$-axis and angle priority saturation conditions maintains a sinusoidal curve, contrary to the cosinusoidal actual output power.

Table 2 summarizes the results obtained from Section III and the experimental validation underlying the main characteristics of the virtual power feedback for the three limitation strategies.

## VI. CONCLUSION

This article demonstrated the improvement in the VSG transient stability achieved by implementing the virtual power feedback. The virtual power angle curves are analytically derived and analyzed considering the most adopted limitation strategies. The qualitative stability analysis is validated experimentally by applying a $-0.7$ p.u. symmetrical voltage sag. The experimental results are consistent with theoretical considerations, demonstrating the significant improvement in transient stability obtained with the virtual power feedback for the three limitation strategies. With the $d$-axis technique, the VSG algorithm can virtually inject a higher transmissible power, remarkably reducing the rotor angle acceleration than when utilizing the measured power feedback. In contrast with the measured power, the virtual power features a sinusoidal power-angle curve with $q$-axis and angle priority techniques, thus allowing the control to maintain synchronism after the fault without modifying the control structure. Notably, no

additional dedicated control units are required to avoid the unstable operating conditions caused by the cosine output power behavior. Therefore, virtual power feedback represents a robust and straightforward concept that enhances the VSG transient stability independently of the adopted limitation strategy without modifying the control algorithm or requiring fault detection capability.

## APPENDIX

The virtual current can be calculated considering the virtual equivalent circuit in Fig. 4(a). In the synchronous reference frame, the circuital equations are as follows:

$$e_{v,d} - R_v i_{v,d} + X_v i_{v,q} - v_{v,d} = 0 \tag{38}$$

$$e_{v,q} - R_v i_{v,q} - X_v i_{v,d} - v_{v,q} = 0. \tag{39}$$

Then, (38) can be written, as shown in the following equation:

$$i_{v,q} = -\frac{e_{v,d}}{X_v} + \frac{v_{g,d}}{X_v} + \frac{R_v}{X_v} i_{v,d}. \tag{40}$$

Next, the obtained expression for $i_{v,q}$ is substituted in (39), thus deriving the relation in (10). Note that $i_{v,q}$ is calculated with the same procedure, thereby obtaining (11).

## REFERENCES


[1] U. Tamrakar, D. Shrestha, M. Maharjan, B. P. Bhattarai, T. M. Hansen, and R. Tonkoski, "Virtual inertia: Current trends and future directions," *Appl. Sci.*, vol. 7, no. 7, pp. 654–682, 2017.

[2] nationalgridESO, "GC0137: Minimum specification required for provision of GB grid forming (GBGF) apability (formerly virtual synchronous machine/VSM capability)," National Grid Electricity System Operator Limited, Warwick, West Midlands, U.K., Tech. Rep. GC0137, Mar. 2021. Accessed: Jul. 12, 2025. [Online]. Available: https://www.neso.energy/document/189381/download

[3] ENTSO-E, "Frequency stability in long-terms scenarios and relevant requirement," European Network of Transmission System Operators for Electricity, Brussels, Belgium, Tech. Rep. 211203, Dec. 2021. Accessed: Jul. 12, 2025. [Online]. Available: https://eepublicdownloads.azureedge.net/clean-documents/Publications/ENTSOE%20general%20publications/211203_Long_term_frequency_stability_scenarios_for_publication.pdf

[4] Terna, "Code for transmission dispatching. development and security of the grid," *Grid Code*, Mar. 2023. Accessed: Jul. 11, 2025. [Online]. Available: https://www.terna.it/en/electricsystem/grid-codes/italian-grid-code

[5] C. Li, Y. Yang, Y. Li, Y. Liu, and F. Blaabjerg, "Modeling for oscillation propagation with frequency-voltage coupling effect in grid-connected virtual synchronous generator," *IEEE Trans. Power Electron.*, vol. 40, no. 1, pp. 82–86, Jan. 2025.

[6] C. Li, Y. Yang, and F. Blaabjerg, "Mechanism analysis for oscillation transferring in grid-forming virtual synchronous generator connected to power network," *IEEE Trans. Ind. Electron.*, vol. 72, no. 8, pp. 8715–8720, Aug. 2025.

[7] M. Chen, D. Zhou, and F. Blaabjerg, "Modelling, implementation, and assessment of virtual synchronous generator in power systems," *J. Modern Power Syst. Clean Energy*, vol. 8, no. 3, pp. 399–411, 2020.

[8] V. Mallemaci, F. Mandrile, S. Rubino, A. Mazza, E. Carpaneto, and R. Bojoi, "A comprehensive comparison of virtual synchronous generators with focus on virtual inertia and frequency regulation," *Electric Power Syst. Res.*, vol. 201, 2021, Art. no. 107516.

[9] J. Liu, Y. Miura, and T. Ise, "Comparison of dynamic characteristics between virtual synchronous generator and droop control in inverter-based distributed generators," *IEEE Trans. Power Electron.*, vol. 31, no. 5, pp. 3600–3611, May 2015.

[10] F. Mandrile, E. Carpaneto, and R. Bojoi, "Grid-feeding inverter with simplified virtual synchronous compensator providing grid services and grid support," *IEEE Trans. Ind. Appl.*, vol. 57, no. 1, pp. 559–569, Jan. 2020.

[11] Y. Park, S. Choi, G. Heo, and G.-S. Seo, "Peak shaving control for a virtual synchronous generator in island grids," *IEEE Trans. Smart Grid*, vol. 16, no. 2, pp. 890–902, Mar. 2025.

[12] M. G. Taul, X. Wang, P. Davari, and F. Blaabjerg, "Current limiting control with enhanced dynamics of grid-forming converters during fault conditions," *IEEE Trans. Emerg. Sel. Topics Power Electron.*, vol. 8, no. 2, pp. 1062–1073, Feb. 2020.

[13] L. Huang, H. Xin, Z. Wang, L. Zhang, K. Wu, and J. Hu, "Transient stability analysis and control design of droop-controlled voltage source converters considering current limitation," *IEEE Trans. Smart Grid*, vol. 10, no. 1, pp. 578–591, Jan. 2019.

[14] T. Qoria, F. Gruson, F. Colas, X. Kestelyn, and X. Guillaud, "Current limiting algorithms and transient stability analysis of grid-forming VSCs," *Electric Power Syst. Res.*, vol. 189, 2020, Art. no. 106726.

[15] H. Xin, L. Huang, L. Zhang, Z. Wang, and J. Hu, "Synchronous instability mechanism of p-f droop-controlled voltage source converter caused by current saturation," *IEEE Trans. Power Syst.*, vol. 31, no. 6, pp. 5206–5207, Jun. 2016.

[16] K. G. Saffar, S. Driss, and F. B. Ajaei, "Impacts of current limiting on the transient stability of the virtual synchronous generator," *IEEE Trans. Power Electron.*, vol. 38, no. 2, pp. 1509–1521, Feb. 2022.

[17] C. Shen et al., "Transient stability and current injection design of paralleled current-controlled VSCs and virtual synchronous generators," *IEEE Trans. Smart Grid*, vol. 12, no. 2, pp. 1118–1134, Feb. 2020.

[18] J. Alipoor, Y. Miura, and T. Ise, "Power system stabilization using virtual synchronous generator with alternating moment of inertia," *IEEE J. Emerg. Sel. Topics Power Electron.*, vol. 3, no. 2, pp. 451–458, Feb. 2014.

[19] W. Zhao, L. Wang, W. Song, X. Zhang, and Z. Wang, "Variable inertias of wind turbines in interconnected power system for transient stability enhancement," in *Proc. IEEE 6th Inf. Technol. Mechatron. Eng. Conf.*, vol. 6, 2022, pp. 812–816.

[20] M. Li et al., "Analysis and improvement of large-disturbance stability for grid-connected VSG based on output impedance optimization," *IEEE Trans. Power Electron.*, vol. 37, no. 8, pp. 9807–9826, Aug. 2022.

[21] P. Ge, F. Xiao, C. Tu, Q. Guo, J. Gao, and Y. Song, "Comprehensive transient stability enhancement control of a VSG considering power angle stability and fault current limitation," *CSEE J. Power Energy Syst.*, 2022.

[22] Y. Ma, F. Wang, and L. M. Tolbert, "Virtual synchronous generator with limited current–impact on system transient stability and its mitigation," in *Proc. IEEE Energy Convers. Congr. Expo.*, 2020, pp. 2773–2778.

[23] C. Luo, X. Ma, T. Liu, and X. Wang, "Controller-saturation-based transient stability enhancement for grid-forming inverters," *IEEE Trans. Power Electron.*, vol. 38, no. 2, pp. 2646–2657, Feb. 2022.

[24] S. Kim, K.-H. Kim, S. Cui, and J.-J. Jung, "Enhancement methods for transient stability of grid-forming converters with low damping," in *Proc. Energy Convers. Congr. Expo. Eur.*, 2024, pp. 1–7.

[25] A. Camboni, V. Mallemaci, F. Mandrile, and R. Bojoi, "Transient stability improvement of virtual synchronous generators under current limitation: The benefits of virtual power feedback," in *Proc. IEEE Energy Conver. Congr. Expo.*, 2024, pp. 1002–1009.

[26] F. Blaabjerg, *Control of Power Electronic Converters and Systems*, vol. 2. Cambridge, MA, USA: Academic, 2018.

[27] S. N. Vukosavic, *Grid-Side Converters Control and Design*. Berlin, Germany: Springer, 2018.

[28] F. Mandrile, V. Mallemaci, E. Carpaneto, and R. Bojoi, "Lead-lag filter-based damping of virtual synchronous machines," *IEEE Trans. Ind. Appl.*, vol. 59, no. 6, pp. 6900–6913, Jun. 2023.

[29] F. Mandrile, E. Carpaneto, E. Armando, and R. Bojoi, "Simple tuning method of virtual synchronous generators reactive control," in *Proc. IEEE Energy Convers. Congr. Expo.*, 2020, pp. 2779–2785.

[30] X. Wang, Y. W. Li, F. Blaabjerg, and P. C. Loh, "Virtual-impedance-based control for voltage-source and current-source converters," *IEEE Trans. Power Electron.*, vol. 30, no. 12, pp. 7019–7037, Dec. 2014.

[31] J. He and Y. W. Li, "Analysis, design, and implementation of virtual impedance for power electronics interfaced distributed generation," *IEEE Trans. Ind. Appl.*, vol. 47, no. 6, pp. 2525–2538, Jun. 2011.

[32] P. Kundur, *Power System Stability*. New York, NY, USA: McGraw-Hill Education, Jan. 1994.

[33] F. Zhao, Z. Shuai, C. Shen, H. Cheng, and Y. Shen, "Comparison of transient angle stability between different virtual synchronous generators," in *Proc. IEEE 3rd Conf. Energy Internet Energy Syst. Integration*, 2019, pp. 2529–2533.
[34] H. Wu and X. Wang, "A mode-adaptive power-angle control method for transient stability enhancement of virtual synchronous generators," *IEEE J. Emerg. Select. Topics Power Electron.*, vol. 8, no. 2, pp. 1034–1049, Aug. 2020.
[35] A.-A. Fouad and V. Vittal, *Power System Transient Stability Analysis Using the Transient Energy Function Method*. London, U.K.: Pearson Education, 1991.
[36] R. Teodorescu, M. Liserre, and P. Rodriguez, *Grid Converters for Photovoltaic and Wind Power Systems*. Hoboken, NJ, USA: Wiley, 2011.

**ALESSIA CAMBONI** (Student Member, IEEE) was born in Sassari, Italy, in 1999. She received the B.S. and M.S. degrees in electrical engineering in 2020 and 2023, respectively, from the Politecnico di Torino, Torino, Italy, where she is currently working toward the Ph.D. degree with Dipartimento Energia "G. Ferraris." "Her Ph.D topic relates to the stability of virtual synchronous machines and control for power electronic grid-connected applications."

**VINCENZO MALLEMACI** (Member, IEEE) was born in Messina, Italy, in 1996. He received the B.S. and M.S. degrees in electrical engineering from the Politecnico di Torino, Torino, Italy, in 2018 and 2020, respectively, and the Ph.D. degree in electrical engineering from Dipartimento Energia "G. Ferraris," Politecnico di Torino, in 2024.

His research interests include virtual synchronous machines and control for power electronic grid-connected converters.

**FABIO MANDRILE** (Member, IEEE) received the M.Sc. and Ph.D. degrees in electrical engineering from the Politecnico di Torino, Torino, Italy, in 2017 and 2021, respectively.

He is currently an Assistant Professor with Dipartimento Energia "G. Ferraris," Politecnico di Torino. His research interests include virtual synchronous machines and power electronics for grid-connected applications, the experimental characterization of converters, and motor drives.

**RADU BOJOI** (Fellow, IEEE) received the M.Sc. degree in electrical engineering from the Technical University of Iasi, Iasi, Romania, in 1993 and the Ph.D. degree in electrical engineering from the Politecnico di Torino, Torino, Italy, in 2002.

He is currently a Full Professor of Power Electronics and Electrical Drives with the Energy Department "G. Ferraris" and Chairman of the Power Electronics Innovation Center, Politecnico di Torino. He has authored or coauthored more than 200 papers covering electrical drives and power electronics for industrial applications, transportation electrification, power quality, and home appliances. He is involved in many research projects with industry aiming at obtaining new products involving emerging technologies.

Dr. Bojoi was the Co-Editor-In-Chief of IEEE TRANSACTIONS ON INDUSTRIAL ELECTRONICS. He was the recipient of ten IEEE paper awards.